



Preparation of solid-state Z-scheme $\text{Bi}_2\text{MoO}_6/\text{MO}$ ($\text{M}=\text{Cu}$, $\text{Co}_{3/4}$, or Ni) heterojunctions with internal electric field-improved performance in photocatalysis

Haiping Li^a, Tingxia Hu^b, Renjie Zhang^b, Jianqiang Liu^c, Wanguo Hou^{a,b,*}

^a National Engineering Research Center for Colloidal Materials, Shandong University, Jinan 250100, PR China

^b Key Laboratory for Colloid and Interface Chemistry (Ministry of Education), Shandong University, Jinan 250100, PR China

^c School of Physics, Shandong University, Jinan 250100, PR China

ARTICLE INFO

Article history:

Received 16 December 2015

Received in revised form 30 January 2016

Accepted 4 February 2016

Available online 6 February 2016

Keywords:

Bismuth molybdate

Cupric oxide

Cobaltosic oxide

Heterostructure

Built-in electric field

ABSTRACT

Up to now, studies on solid-state Z-scheme two-component heterojunctions have hardly referred to roles of interfacial internal electric fields (IEFs). Herein, solid-state Z-scheme $\text{Bi}_2\text{MoO}_6/\text{MO}$ ($\text{M}=\text{Cu}$, $\text{Co}_{3/4}$, or Ni) heterojunction photocatalysts were simply synthesized, for the first time, with enhanced photocatalytic performance toward organic degradation. Electron microscopy images reveal that the MO homogeneously distributes on surfaces of the Bi_2MoO_6 hierarchical microspheres, and they close contact with distinct heterojunction interfaces. X-ray photoelectron spectra (XPS) suggest that the electron transfer occurs between the Bi_2MoO_6 and MO after they contact, resulting in formation of IEFs at their interfaces. Based on band gap values and valance-band XPS and ultraviolet photoelectron spectra, energy band levels of the Bi_2MoO_6 and MO are defined, and directions of the interfacial IEFs are determined. The IEFs play key roles for the formation of the Z-scheme $\text{Bi}_2\text{MoO}_6/\text{MO}$ heterojunctions and for the photoactivity enhancement. This work provides a better insight into the formation mechanism of solid-state two-component Z-scheme heterojunctions and a significant experimental guidance for studying other similar systems.

© 2016 Elsevier B.V. All rights reserved.

1. Introduction

Solar energy-driven semiconductor photocatalysis is a promising technology to alleviate global energy crisis by reducing CO_2 and H_2O to generate hydrocarbon fuels and H_2 , respectively, and to remedy environmental contamination by degrading toxic contaminants [1,2]. However, industrial application of this technology is seriously limited by low performance of current photocatalysts which is primarily caused by high recombination efficiency of photogenerated charge carriers [3]. To enhance the photocatalytic performance, many methods have been developed, such as morphological accommodation, elemental doping, crystal engineering, and heterojunction/composite construction [4–7]. Among them, the construction of heterojunctions attracts the most interest of scientists, because, for the heterojunctions, photogenerated electron (e^-) transfer between conduct bands (CBs) as well as hole

(h^+) transfer between valance bands (VBs) of two photocatalysts considerably increase the separation efficiency of photogenerated charge carriers (SEPC), favoring the photoactivity improvement [7]. However, reducibility and oxidizability of corresponding e^- and h^+ are both weakened, consequently decreasing the photocatalytic performance. Hence, it is commonly difficult for the traditional heterojunction photocatalysts to simultaneously possess high SEPC and strong redox ability [8].

Z-scheme heterojunctions are good candidates to overcome above problems, and are thereby considered promising for industrial application. In the Z-scheme heterojunctions, CB and VB edge levels of one photocatalyst (PC I) are higher than corresponding ones of the other photocatalysts (PC II). The photogenerated e^- at CB of the PC II transfers to VB of the PC I to recombine with the h^+ there, which leaves more e^- in the PC I and more h^+ in the PC II to participate reduction and oxidation reactions, respectively. Thus, the Z-scheme heterojunctions simultaneously keep high SEPC, high reducibility of the PC I, and high oxidizability of the PC II [8]. Different types of Z-scheme heterojunctions have been developed, including “PC I-mediator-PC II” and all-solid-state “PC I-conductor-PC II” and “PC I-PC II” types [9–11]. The mediator in

* Corresponding author at: National Engineering Research Center for Colloidal Materials, Shandong University, Jinan 250100, PR China.

E-mail address: wghou@sdu.edu.cn (W. Hou).

the “PC I-mediator-PC II” is generally an electron acceptor/donor pair in solution [12], which induces some drawbacks such as backward reactions and shielding incident light. The all-solid-state types can avert these drawbacks [8]. Two-component “PC I-PC II”-type Z-scheme photocatalysts are attracting a great deal of interest [10,13–23]. However, research on formation mechanisms of these Z-scheme heterojunctions is still very superficial. Only a few studies referred to energy band shifts of the PC I and PC II after they contact [10,14,19], and roles of the interfacial IEFs [7,24] have not been reported yet.

Bi_2MoO_6 , a typical Aurivillius oxide, is a promising visible-light-driven photocatalyst for photodegradation of organics [25] and oxygen evolution [26]. Photocatalytic performance of Bi_2MoO_6 can be improved significantly via construction of heterojunctions, such as $\text{TiO}_2/\text{Bi}_2\text{MoO}_6$ [27], $\text{Bi}_{3.64}\text{Mo}_{0.36}\text{O}_{6.55}/\text{Bi}_2\text{MoO}_6$ [28], $\text{g-C}_3\text{N}_4/\text{Bi}_2\text{MoO}_6$ [29], and layered double hydroxide/ Bi_2MoO_6 [30]. However, there are few reports focused on Bi_2MoO_6 heterojunctions containing cost-effective transition metal oxide (e.g. CuO , Co_3O_4 , and NiO), even though they seem to display matched energy band levels [24,29,31,32]. Moreover, few Bi_2MoO_6 -containing Z-scheme heterojunctions were synthesized so far [33,34].

In this study, solid-state Z-scheme $\text{Bi}_2\text{MoO}_6/\text{MO}$ ($\text{M}=\text{Cu}$, $\text{Co}_3/4$, or Ni) photocatalysts were prepared for the first time. They exhibit enhanced photocatalytic performance toward degradations of rhodamine B (RhB) and sulforhodamine B (SRhB), compared with single Bi_2MoO_6 . The photoactivity enhancement benefits from the IEFs, formed at the $\text{Bi}_2\text{MoO}_6/\text{MO}$ interfaces, which increases the SEPC. This work not only provides new Z-scheme photocatalysts with improved performance, but also gives a better insight into the formation mechanism of solid-state two-component Z-scheme heterojunctions.

2. Experimental

2.1. Materials

$\text{Bi}(\text{NO}_3)_3 \cdot 5\text{H}_2\text{O}$, $\text{Na}_2\text{MoO}_4 \cdot 2\text{H}_2\text{O}$, $\text{Cu}(\text{NO}_3)_2 \cdot 3\text{H}_2\text{O}$, $\text{CoCl}_2 \cdot 6\text{H}_2\text{O}$, $\text{Ni}(\text{NO}_3)_2 \cdot 6\text{H}_2\text{O}$ and NaOH were purchased from Aladdin (Shanghai, P. R. China). Commercial N doped TiO_2 (N-TiO_2) with an N content of ~4% was purchased from Xuan Cheng Jing Rui New Material Co., Ltd. (P. R. China). Water with a specific resistivity of $18.2 \text{ M}\Omega \cdot \text{cm}$ was prepared through a Hitech-Kflow water purification system (Shanghai, P. R. China).

2.2. Preparation of Bi_2MoO_6 hierarchical microspheres

Bi_2MoO_6 hierarchical microspheres were prepared by a reported method [35]. In brief, 1.6866 g of $\text{Bi}(\text{NO}_3)_3 \cdot 5\text{H}_2\text{O}$ and 0.4206 g of $\text{Na}_2\text{MoO}_4 \cdot 2\text{H}_2\text{O}$ were dissolved in 5 mL of ethylene glycol, respectively. Then, the two solutions were mixed together, and 20 mL of ethanol was slowly dropped into the mixture, followed by stirring for 10 min. The resultant clear solution was transferred into a 50 mL Teflon-lined stainless steel autoclave and heated at 160°C for 10 h. Subsequently, the autoclave was cooled naturally to the room temperature. The samples were obtained after filtration, washed with water and ethanol for three times, dried at 80°C for 24 h in air, and annealed at 400°C for 3 h.

2.3. Preparation of $\text{Bi}_2\text{MoO}_6/\text{MO}$ composites

Bi_2MoO_6 powders (0.1 g) were dispersed in 20 mL of $\text{Cu}(\text{NO}_3)_2$, CoCl_2 , or $\text{Ni}(\text{NO}_3)_2$ solution whose concentration was designed according to the expected MO content in the final $\text{Bi}_2\text{MoO}_6/\text{MO}$ composite. The pH of the $\text{Bi}_2\text{MoO}_6/\text{M}^{2+}$ aqueous suspension was adjusted to 7.0 for $\text{Bi}_2\text{MoO}_6/\text{Cu}^{2+}$ and to 10.0 for $\text{Bi}_2\text{MoO}_6/\text{Co}^{2+}$ and

$\text{Bi}_2\text{MoO}_6/\text{Ni}^{2+}$, using 0.1 M NaOH solution under stirring. The resultant precipitate (precursor) was collected after filtration, washed with water for several times, and dried at 80°C for 24 h. The target $\text{Bi}_2\text{MoO}_6/\text{MO}$ composite was gained after calcining the precursor in air, at 300°C for 4 h for $\text{Bi}_2\text{MoO}_6/\text{CuO}$ and $\text{Bi}_2\text{MoO}_6/\text{Co}_3\text{O}_4$, and at 250°C for 2 h for $\text{Bi}_2\text{MoO}_6/\text{NiO}$.

Fig. 1 shows the preparation procedure of the $\text{Bi}_2\text{MoO}_6/\text{MO}$ composites. For simplicity, the as-prepared $\text{Bi}_2\text{MoO}_6/\text{CuO}$ composites with CuO contents of 0.2, 0.3, and 0.4 wt.% are denoted as Bi/Cu-2, Bi/Cu-3, and Bi/Cu-4, respectively; the $\text{Bi}_2\text{MoO}_6/\text{Co}_3\text{O}_4$ composites with Co_3O_4 contents of 0.1, 0.2, and 0.3 wt.% are signified as Bi/Co-1, Bi/Co-2, and Bi/Co-3, respectively; the $\text{Bi}_2\text{MoO}_6/\text{NiO}$ composites with NiO contents of 0.1, 0.2, and 0.3 wt.% are symbolized as Bi/Ni-1, Bi/Ni-2, and Bi/Ni-3, respectively. For comparison, CuO , Co_3O_4 , and NiO were prepared through a similar process without addition of the Bi_2MoO_6 .

2.4. Characterizations

Powder X-ray diffraction (XRD) was performed on a D8 Advance diffractometer (Bruker, Germany) with $\text{Cu K}\alpha$ radiation ($\lambda = 1.54184 \text{ \AA}$). X-ray photoelectron spectroscopy (XPS) test was carried out on a Thermo Scientific Escalab 250Xi spectrometer (UK) with $\text{Al K}\alpha$ radiation. The C 1s peak at 284.6 eV was used to calibrate peak positions. Ultraviolet photoelectron spectra (UPS) of samples were measured on the same instrument with He I (21.22 eV) as excitation source at an applied bias voltage of 8 eV. Morphological observation was performed on a Supra55 field emission-scanning electron microscope (SEM, Zeiss, Germany), a JEM-1011 transmission electron microscope (TEM, Jeol, Japan), and a JEM-2100F high-resolution TEM (HRTEM, Jeol, Japan). The spatial elemental distributions of composites were investigated by EDS (energy dispersive spectrometer, equipped in the SEM instrument) elemental mapping analysis. Selected area electron diffraction (SAED) patterns were obtained from the HRTEM. UV-vis diffuse reflectance spectra were measured using a U-4100 spectrophotometer (Hitachi, Japan), with a BaSO_4 reference. Photoluminescence (PL) spectra were measured using an F-7000 spectrophotometer (Hitachi, Japan) at an excitation wavelength of 400 nm, and excitation and emission slit widths of 5 and 7 nm, respectively. Time-resolved fluorescence decay spectra were recorded on an FLS920 time-resolved spectrofluorometer (Edinburgh Analytical Instruments, UK) using the time-correlated single photon counting method, excited with a picosecond pulsed diode laser (EPL-375) at 377.8 nm, and monitored at 460 nm. N_2 adsorption-desorption isotherms were measured on a Quantachrome NOVA2000E instrument (USA) at liquid nitrogen temperature. Samples were degassed at 150°C for 3 h under vacuum before measurement.

Photocatalytic performance of as-prepared photocatalysts was evaluated by degrading the RhB and SRhB at room temperature, on a XPA-7 photocatalytic reaction apparatus (Xujiang Electromechanical Plant, Nanjing, P. R. China) [36]. A 500 W Xe lamp, equipped with an ultraviolet cutoff filter ($\lambda \geq 420 \text{ nm}$), was used as the visible light source. For each run, 0.05 g of photocatalyst was added to 50 mL of the RhB or SRhB solution (10 mg/L). Prior to irradiation, the suspension was stirred in dark for 1 h to ensure sorption equilibrium. After given irradiation times, ~4 mL of the suspensions were taken out and filtered through $0.45\text{-}\mu\text{m}$ polyether sulfone membranes. Absorbance of the filtrates was measured by a Hewlett-Packard 8453 UV-vis spectrophotometer (USA) at 554 nm for the RhB and 565 nm for the SRhB. The ratio of remaining dye concentration to its initial concentration (C/C_0) is equal to the ratio of corresponding absorbances.

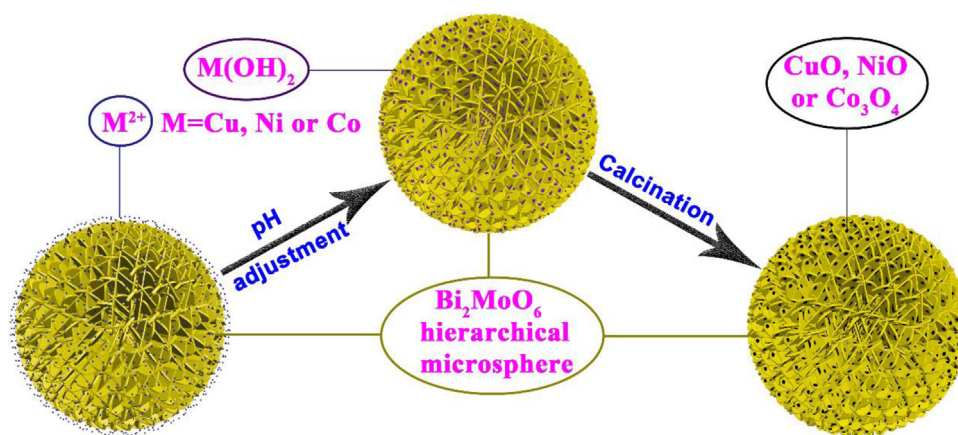


Fig. 1. Schematic preparation and structure of $\text{Bi}_2\text{MoO}_6/\text{MO}$ ($\text{M} = \text{Cu}$, $\text{Co}_{3/4}$, or Ni) composites.

3. Results and discussion

3.1. Structures and morphologies

XRD patterns of the Bi_2MoO_6 , CuO , Co_3O_4 , and NiO samples (Fig. S1, Supporting information) show clear diffraction peaks indexed well to orthorhombic Bi_2MoO_6 (JCPDS file No. 21-0102), monoclinic CuO (JCPDS file No. 89-5897), cubic Co_3O_4 (JCPDS file No. 42-1467), and cubic NiO (JCPDS file No. 89-5881) structures, respectively. XRD patterns of the composites Bi/Cu-3 , Bi/Co-3 , and Bi/Ni-2 all show similar diffraction peaks as the Bi_2MoO_6 . Namely, no peaks of the MO are observed due to its low content in the composite.

Survey XPS spectra (Fig. 2a–c) indicate that the Bi/Cu-3 , Bi/Co-2 , and Bi/Ni-2 samples contain Cu, Co, and Ni, respectively, besides Bi, Mo, O and adventitious C [37]. The calculated molar ratio of O/Bi/Mo for the Bi_2MoO_6 is 6.74/2.00/1, and those of O/M for the CuO , Co_3O_4 , and NiO are 0.98/1, 1.33/1, and 1.07/1, respectively (Table S1, Supporting information), which are all close to the theoretical values. Fig. 2d–f shows M 2p high-resolution XPS spectra of the MO and $\text{Bi}_2\text{MoO}_6/\text{MO}$ composites. Peaks at binding energies (BE) of 953.8 and 933.9 eV in Cu 2p spectra (Fig. 2d), 795.4 and 780.2 eV in Co 2p spectra (Fig. 2e), and 873.1 and 855.6 eV in Ni 2p spectra (Fig. 2f) are ascribed to $\text{M } 2p_{1/2}$ and $\text{M } 2p_{3/2}$ of the CuO , Co_3O_4 , and NiO , respectively [38–41]. These demonstrate successful deposition of the MO on the Bi_2MoO_6 . The MO contents in the composites, obtained from the XPS data, are higher than the theoretical values (Table S1), indicating that the MO distributes on surfaces of the Bi_2MoO_6 . In the Ni 2p spectra (Fig. 2f), appearance of peaks at 872.0 and 854.5 eV results from Ni atoms interacting with surficial oxygen vacancies [42]. Asterisks denote satellite peaks in the figure [38–41]. In Fig. 2g–i, peaks at around 530.1 and 529.7 eV for the Bi_2MoO_6 correspond to O atoms in O–Mo and O–Bi bonds, respectively [29]. Those at 529.8, 530.3, and 530.5 eV for CuO , Co_3O_4 , and NiO are ascribed to O atoms in O–Cu, O–Co, and O–Ni bonds, respectively [43–45], and those at 532.7–532.8 and 531.3 eV are related to adsorbed CO_2 and surficial hydroxyl, respectively [46,47].

Compared with the $\text{M } 2p_{1/2}$ and $\text{M } 2p_{3/2}$ peaks of the MO, those of the Bi/Cu-3 shift by ~ 1.1 eV toward lower BE (Fig. 2d), while those of the Bi/Co-2 and Bi/Ni-2 move by ~ 0.7 and 1.0 eV toward higher BE (Fig. 2e and f), respectively. Similarly, the O 1s peak, corresponding to CuO in the Bi/Cu-3 , shifts by ~ 0.5 eV toward lower BE (Fig. 2g), while those, corresponding to Co_3O_4 in the Bi/Co-2 and NiO in the Bi/Ni-2 , shift by ~ 0.1 and 0.2 eV toward higher BE, respectively (Fig. 2h and i), in comparison with the O 1s peaks of the MO .

The decrease/increase in BE of XPS peaks of semiconductors can be caused by the increase/decrease in electron density on their surfaces, and the electron density variation can be achieved via electron transfers between different semiconductors [48–50]. Generally, electrons transfer from semiconductors with lower work function (ϕ) to those with higher ϕ , until a united Fermi level is formed [10,51]. UPS spectra of Bi_2MoO_6 and MO were measured to determine the ϕ . As shown in Fig. 3, the secondary cut-off region ($E_{\text{cut-off}}$) and Fermi energy (E_{Fermi}) are clearly defined through inter-sections of lines, and the ϕ is calculated via the equation $\phi = h\nu - E_{\text{cut-off}} + E_{\text{Fermi}}$, where $h\nu$ (21.22 eV) is the incoming photon energy from the He I source [52,53]. The ϕ of Bi_2MoO_6 , CuO , Co_3O_4 , and NiO samples are ~ 5.07 , 5.27, 4.54, and 4.97 eV, respectively. The order, $\phi(\text{Co}_3\text{O}_4) < \phi(\text{NiO}) < \phi(\text{Bi}_2\text{MoO}_6) < \phi(\text{CuO})$ suggests that after contact of the Bi_2MoO_6 with the MO, the electrons would transfer from Bi_2MoO_6 to CuO for $\text{Bi}_2\text{MoO}_6/\text{CuO}$, from Co_3O_4 to Bi_2MoO_6 for $\text{Bi}_2\text{MoO}_6/\text{Co}_3\text{O}_4$, and from NiO to Bi_2MoO_6 for $\text{Bi}_2\text{MoO}_6/\text{NiO}$, leading to a decrease of surficial electron density of the former and an increase of the latter, which thereby causes the shifts of the M 2p (Fig. 2d–f) and O 1s peaks (Fig. 2g–i). However, there are not corresponding peak shifts observed in Bi 4f and Mo 3d spectra of the samples (Fig. S2a, b, Supporting information). This is probably because the contents of the MO in the composites are too low to induce detectable electron density variation for Bi_2MoO_6 .

The Bi_2MoO_6 microspheres are composed of irregular nanosheets (Figs. S3 and S4a, Supporting information), showing similar hierarchical morphology as reported [35]. The $\text{Bi}_2\text{MoO}_6/\text{MO}$ composites retain the morphology of the Bi_2MoO_6 except breakage of a few microspheres in preparation processes (Fig. 4a–c). Though the pure CuO shows rod-like morphology, and the pure Co_3O_4 and NiO reveal small nanosheet structures (Fig. S4b–d), they all uniformly deposit on the surfaces of the Bi_2MoO_6 microspheres as nanoparticles of several to tens of nanometers (Figs. 4 d–g and S5 in supporting information). HRTEM images show that the MO close contacts the Bi_2MoO_6 with distinct interfaces (Fig. 4d–f). The lattice fringes with spacings of 0.325 (Fig. 4d), 0.276 (Fig. 4e), and 0.202 nm (Fig. 4f) are ascribed to (140), (200), and (080) planes of Bi_2MoO_6 , while those with spacings of 0.342 (Fig. 4d), 0.234 (Fig. 4e), and 0.191 nm (Fig. 4f) correspond to (010) facets of CuO [54], (222) facets of Co_3O_4 , and (331) facets of NiO , respectively. Selected area electron diffraction (SAED) patterns (Fig. S6, Supporting information) indicates that both the Bi_2MoO_6 nanosheets assembling the microspheres and the MO nanoparticles are single crystal structures. The HRTEM and SAED data demonstrate that the Bi_2MoO_6 nanosheets expose (001) facets at top and bottom surfaces and (010), (100) and (140) facets at side surfaces (Fig. 4h).

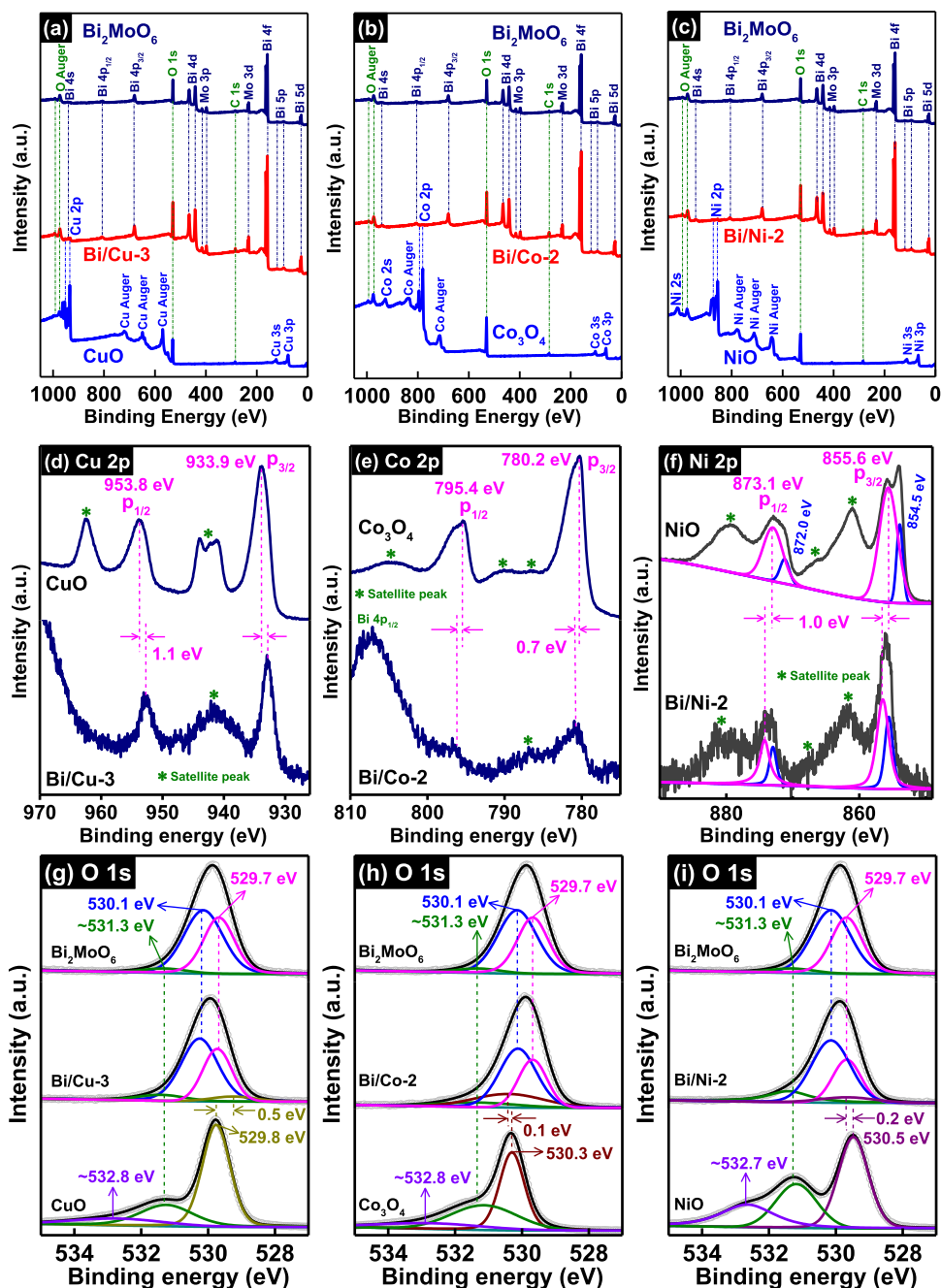


Fig. 2. (a–c) Survey XPS spectra and high-resolution XPS spectra of (d) Cu 2p, (e) Co 2p, (f) Ni 2p, and (g–i) O 1s for Bi_2MoO_6 , CuO , Co_3O_4 , NiO and their composites.

3.2. Photoabsorption performance

UV–vis reflectance diffraction spectra (Fig. 5a) show that visible-light absorption of the $\text{Bi}_2\text{MoO}_6/\text{MO}$ composites is slightly stronger than the pure Bi_2MoO_6 , which is probably because of strong photoabsorption of the MO in visible and even near-infrared regions (Fig. 5b). Band gaps (E_g) of semiconductors were generally calculated using the equation $\alpha h\nu = A(h\nu - E_g)^{n/2}$ where h , α , ν , A , and n are the Planck constant, the absorption coefficient, the light frequency, the proportionality constant, and a parameter depending on transition nature of a semiconductor, respectively. $n = 1$ means a direct band-gap transition, while $n = 4$ suggests an indirect one [30]. $n = 4$ and $n = 1$ are suitable for the Bi_2MoO_6 [55] and MO [56–58], respectively. E_g of the Bi_2MoO_6 , CuO , Co_3O_4 , and NiO samples are determined to be 2.48, 1.38, 1.72, and 2.50 eV, respectively, from

the $(ah\nu)^{2/n}$ vs $h\nu$ curves (Fig. 5c), which are close to reported values [30,59–61], except that the E_g of the NiO is lower than the reported value (~ 3.6 eV) in literature [62,63]. The $(ah\nu)^2$ vs $h\nu$ curve for the Co_3O_4 exhibits two sections of linear relationship with E_g of 1.72 eV and 1.22 eV, respectively, similar as reported [61]. The E_g of 1.72 eV should be associated with charge transfer from O^{2-} to Co^{2+} , while the E_g of 1.22 eV is assigned to charge transfer from O^{2-} to Co^{3+} [61]. On the whole, deposition of the MO on the Bi_2MoO_6 contributes to the photoabsorption enhancement.

3.3. Photocatalytic performance

Photocatalytic performance of the Bi_2MoO_6 , MO and their composites was investigated via photodegradation of the RhB and SRhB

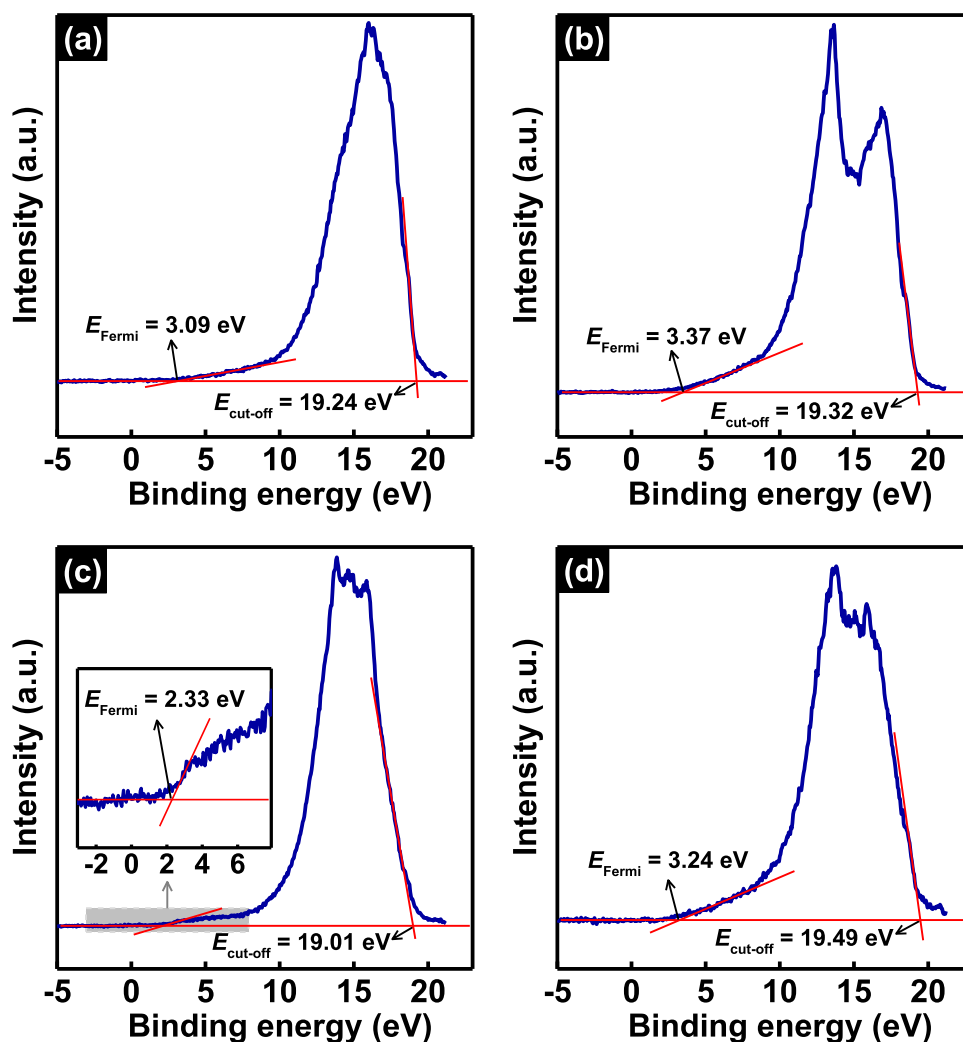
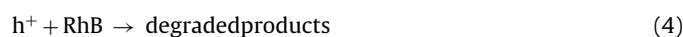
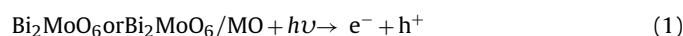


Fig. 3. UPS spectra of (a) Bi_2MoO_6 , (b) CuO , (c) Co_3O_4 , and (d) NiO . Lines are used to determine secondary cut-off region ($E_{\text{cut-off}}$) and Fermi energy (E_{Fermi}).

dyes under visible light irradiation. Adsorption-desorption equilibria of the dyes on/from all of these photocatalysts reached after 60 min (Fig. 6a and b). Photocatalytic efficiencies of the $\text{Bi}_2\text{MoO}_6/\text{MO}$ composites are higher than those of the Bi_2MoO_6 and MO , and also exceed those of commercial N-TiO_2 . The Bi/Cu-3 , Bi/Co-2 , and Bi/Ni-2 composites can photodegrade $\sim 90\%$, 93% , and 66% of the RhB in 140 min and $\sim 21\%$, 32% , and 66% of the SRhB in 570 min, while the Bi_2MoO_6 can only degrade $\sim 51\%$ of the RhB in 140 min and $\sim 17\%$ of the SRhB in 570 min, respectively. The photodegradation data were well fitted (Fig. 6c and d) to a pseudo-first-order kinetic model [36]. Fig. 6e shows the pseudo-first-order kinetic rate constants (k) of various photocatalysts. The k values of the Bi/Cu-3 , Bi/Co-2 , and Bi/Ni-2 are ~ 3.3 , 3.8 , and 1.6 times those of the Bi_2MoO_6 for the RhB degradation and ~ 1.3 , 2.1 , and 4.5 times for the SRhB degradation, respectively. Influences of MO contents in the $\text{Bi}_2\text{MoO}_6/\text{MO}$ composites on the photocatalytic activity were investigated. The photodegradation efficiencies of the RhB on the $\text{Bi}_2\text{MoO}_6/\text{MO}$ composites increase then decrease with increasing MO contents (Fig. S7, Supporting information). Optimal contents of the CuO , Co_3O_4 , and NiO are 0.3 , 0.2 , and 0.2 wt.%, respectively. The photoactivity decrease of the composites containing excessive MO is because the MO with low photoactivity covers active sites on the Bi_2MoO_6 surfaces [27]. Notably, the Bi/Co-2 and Bi/Ni-2 composites exhibit the highest photodegradation efficiencies for the RhB and SRhB, respectively.

Generally, superoxide radicals ($\bullet\text{O}_2^-$), e^- , h^+ , and hydroxyl radicals ($\bullet\text{OH}$) are possible active species to degrade organics [64–66]. To evaluate roles of these active species in photodegradation of the RhB, corresponding scavengers were added to reaction suspensions. The scavengers used for the $\bullet\text{O}_2^-$, e^- , h^+ , and $\bullet\text{OH}$ are benzoquinone (BQ), $\text{K}_2\text{Cr}_2\text{O}_7$, sodium oxalate (Ox), and *tert*-butyl alcohol (*t*-BuOH) [64–66], respectively. Similar results were obtained for the Bi_2MoO_6 and $\text{Bi}_2\text{MoO}_6/\text{MO}$ composites, as shown in Fig. 7. Addition of the *t*-BuOH causes little changes of the photodegradation efficiencies, indicating that the $\bullet\text{OH}$ is not primary active species in the photocatalytic processes. Significant decrease of the photocatalytic efficiencies are observed when the Ox, BQ and $\text{K}_2\text{Cr}_2\text{O}_7$ are added, confirming important roles of the h^+ , $\bullet\text{O}_2^-$, and e^- in the photodegradation reactions. The key role of the e^- is reducing O_2 to $\bullet\text{O}_2^-$ [13,18]. Thus, the photodegradation processes are primarily governed by the h^+ and $\bullet\text{O}_2^-$. Probable reactions are:



Recyclability and stability of the photocatalysts were investigated. After three runs of photocatalytic reactions, the photoactivity of Bi/Cu-3 , Bi/Co-2 , and Bi/Ni-2 prominently decreases (Fig. S8,

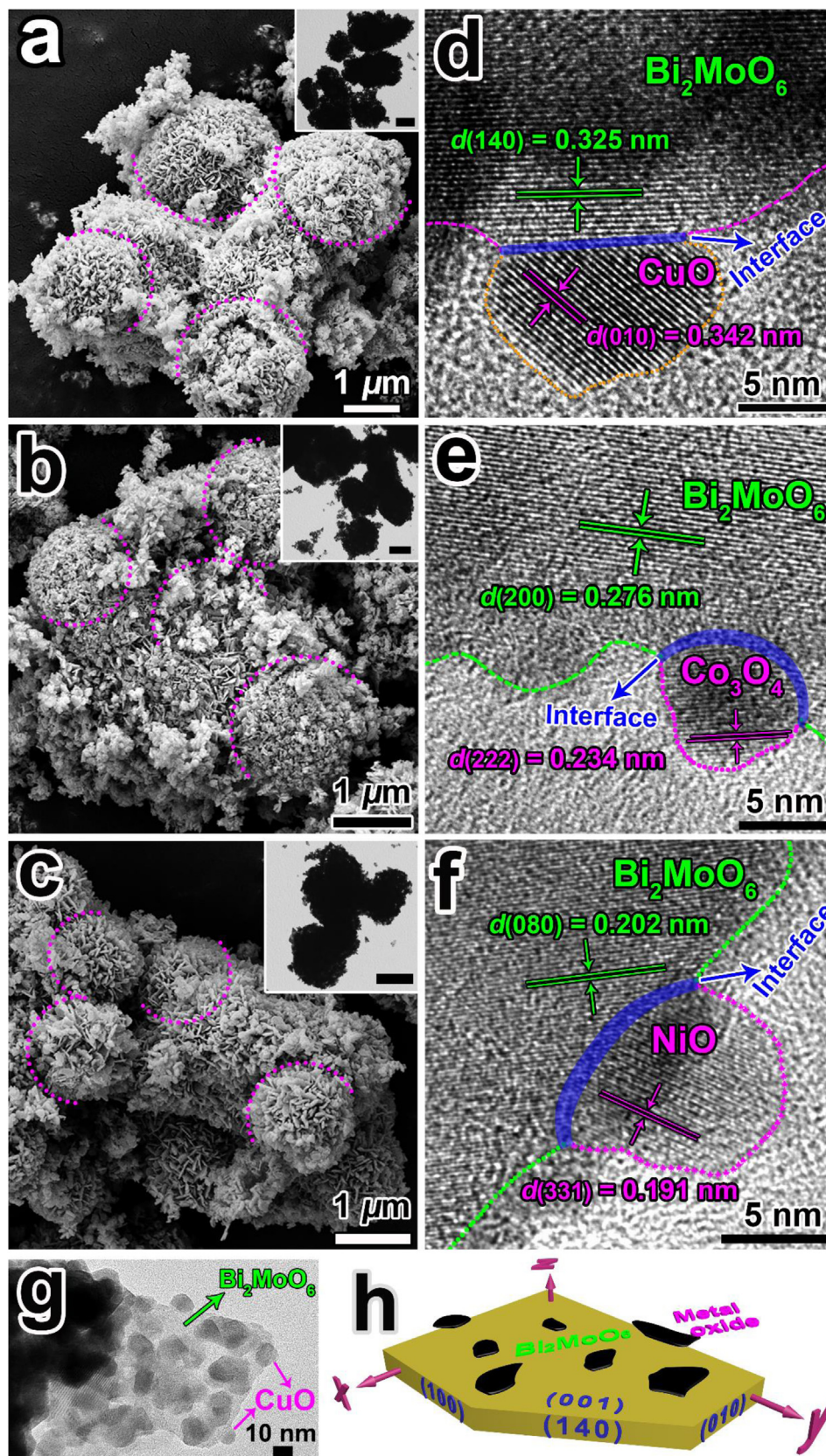


Fig. 4. (a–c) SEM, (g and insets in a–c) TEM, (d–f) HRTEM images and (h) schematic structure of $\text{Bi}_2\text{MoO}_6/\text{MO}$ (M = Cu, $\text{Co}_3/4$, or Ni) composites. Scale bar in insets: 1 μm .

Supporting information). To find out the reason for the photoactivity decrease, the XRD pattern and XPS spectrum of Bi/Ni-2 after the photocatalytic reactions were measured, and compared with

those before the reactions. The XRD patterns before and after the reactions are similar (Fig. S9a, Supporting information), indicating a good chemical stability of Bi_2MoO_6 , but the Ni 2p high-resolution

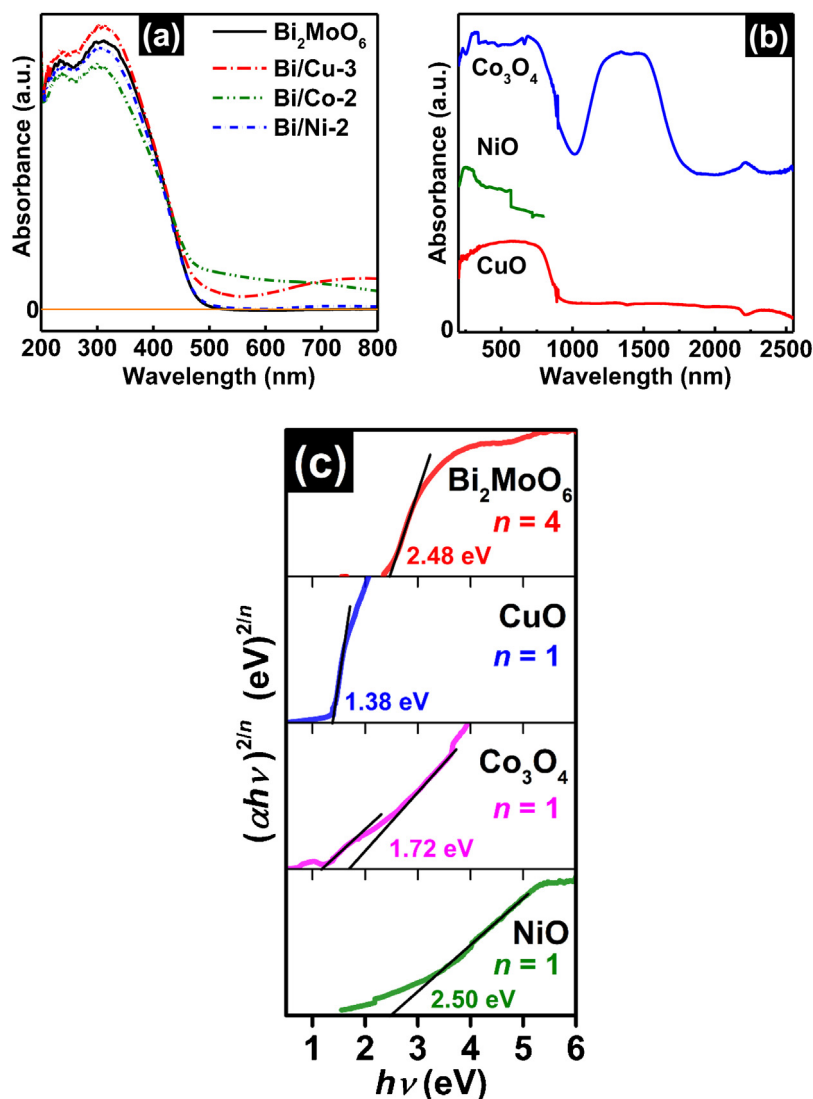


Fig. 5. (a, b) UV–vis diffuse reflectance spectra and (c) corresponding $\alpha h\nu$ vs $h\nu$ curves of Bi₂MoO₆, MO (M = Cu, Co₃/4, or Ni) and their composites. Numbers in the figure are band gaps.

XPS spectrum shows that the NiO amount on the Bi₂MoO₆ surface is considerably reduced (Fig. S9b), which we think results from the dissolution of NiO, in consideration of the quite low content of NiO in the composite. These suggest that the dissolution loss of metal oxide cocatalysts must be considered in the photocatalytic processes, when their loading amounts are much low.

3.4. Photocatalytic mechanism

N₂ adsorption-desorption curves of the Bi₂MoO₆, MO and their composites indicate that all the isotherms are of type IV with type H3 hysteresis loops at high P/P_0 (Fig. S10a and b, Supporting information), featuring slit-shaped mesopores [67]. Brunauer-Emmett-Teller (BET) specific surface areas (S_{BET}) of the Bi₂MoO₆, Bi/Cu-3, Bi/Co-2, and Bi/Ni-2 samples are proximately equal ($24.8 \pm 0.5 \text{ m}^2/\text{g}$), even though those of the CuO ($3.8 \text{ m}^2/\text{g}$), Co₃O₄ ($77.1 \text{ m}^2/\text{g}$), and NiO ($144.7 \text{ m}^2/\text{g}$) samples are quite different. This is because the MO contents in the composites are too low to cause S_{BET} variation of the Bi₂MoO₆. Pore-size distributions of the samples, calculated from the adsorption branches using the Barrett-Joyner-Halenda (BJH) method, all show bimodal pore-size distributions (Fig. S10c). The Bi₂MoO₆, Bi/Cu-3, Bi/Co-2, and Bi/Ni-2

samples possess similar pore sizes, ~ 2.4 and 31.9 nm , suggesting a negligible porous structure change of the Bi₂MoO₆ in the preparation processes of the composites. Appearance of the bimodal pore-size distributions is probably attributed to the hierarchical structures of the samples. The similar S_{BET} and pore sizes manifest that their influences on the photoactivity improvement are negligible. The slight increase in photoabsorption of the Bi₂MoO₆/MO composites (Fig. 5a) should not be a key factor for so prominent photoactivity enhancement either.

Adsorption capacity (Γ_m) of the RhB on the Bi₂MoO₆/MO composites ($1.2\text{--}2.0 \text{ mg/g}$) is less than that on the Bi₂MoO₆ (3.0 mg/g) (Fig. 6a), which demonstrates that the photoactivity enhancement of the composites is irrelevant to the difference in the Γ_m , since low Γ_m generally makes against the photoactivity increase. The Γ_m of the RhB on the samples depend on their Zeta potentials (ζ). The ζ of the Bi₂MoO₆, Bi/Cu-3, Bi/Co-2, Bi/Ni-2, CuO, Co₃O₄, and NiO samples are -11.7 , -1.5 , -10.1 , -7.3 , -0.9 , -0.4 , and 34.1 mV , respectively (Fig. S11, Supporting information). The order of the ζ , $\zeta(\text{Bi}_2\text{MoO}_6) < \zeta(\text{Bi}_2\text{MoO}_6/\text{MO}) < \zeta(\text{MO})$, leads to the order of the Γ_m of RhB, $\Gamma_m(\text{Bi}_2\text{MoO}_6) > \Gamma_m(\text{Bi}_2\text{MoO}_6/\text{MO}) > \Gamma_m(\text{MO})$ (Fig. 6a), since a more positive ζ results in a weaker electrostatic attraction between the RhB (a cationic dye) and particles. However, for the

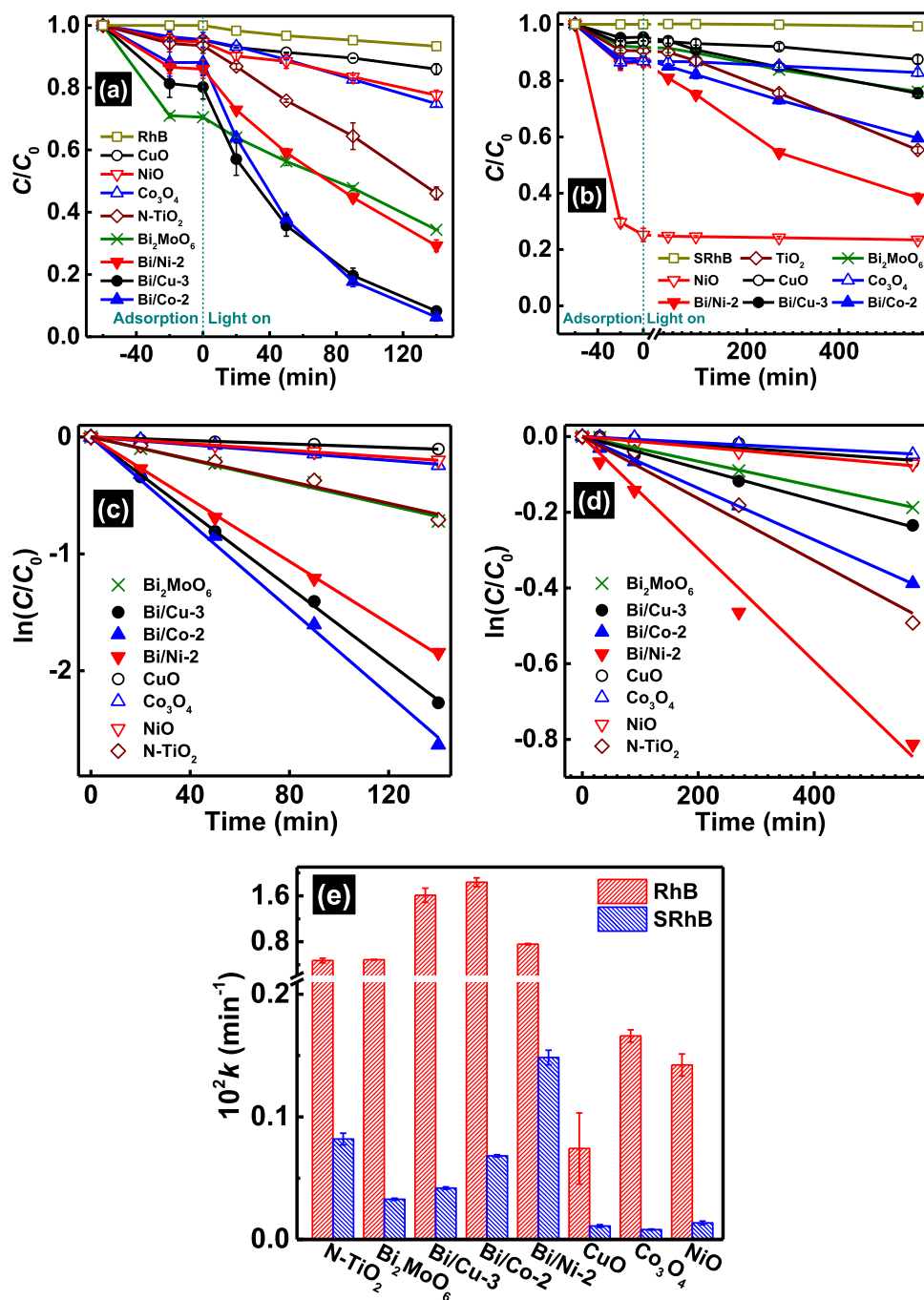


Fig. 6. Adsorption and visible-light photodegradation of (a) RhB and (b) SRhB on various photocatalysts, fitting results of photodegradation data by a pseudo-first-order kinetics model ($-\ln C/C_0 = kt$, where k and t are the pseudo-first-order kinetic rate constant and the photodegradation time, respectively) for (c) RhB and (d) SRhB, and (e) relative k .

SRhB (a zwitterion dye), the positive ζ can increase the electrostatic attraction between anionic groups of the SRhB and particles, so the NiO with the highest ζ and S_{BET} possesses the highest Γ_m of SRhB (7.5 mg/g). The strong adsorption of the SRhB on the NiO makes the $Bi/Ni-2$ have higher Γ_m (1.4 mg/g) than the $Bi/Cu-3$ (0.4 mg/g) and $Bi/Co-2$ (1.2 mg/g) (Fig. 6b). This is probably why the $Bi/Ni-2$ exhibits the highest efficiency for the SRhB photodegradation.

To probe the mechanism of the photoactivity enhancement, photoluminescence (PL) and time-resolved fluorescence decay spectra were measured to indirectly characterize the SEPC [14,68]. The PL spectra show that PL intensities of the composites are all higher than that of the Bi_2MoO_6 , though those of the MO are

quite weak (Fig. 8a), suggesting higher recombination efficiency of photogenerated charge carriers of the composites than that of the Bi_2MoO_6 [14]. The fluorescence decay spectra of the Bi_2MoO_6 and Bi_2MoO_6/MO composites are shown in Fig. 8b. These spectra are well fitted to a two-exponential decay model, as shown by the curves and in Table 1. The short PL lifetime component (τ_1) is related to the surface-related nonradiative recombination processes and the long one (τ_2) is ascribed to recombination of free excitons [68]. Both the τ_1 and τ_2 of the composites are longer than those of the Bi_2MoO_6 (Table 1), suggesting higher SEPC of the composites than that of the Bi_2MoO_6 [69]. The PL and fluorescence decay spectrum results seem contradictory for traditional hetero-

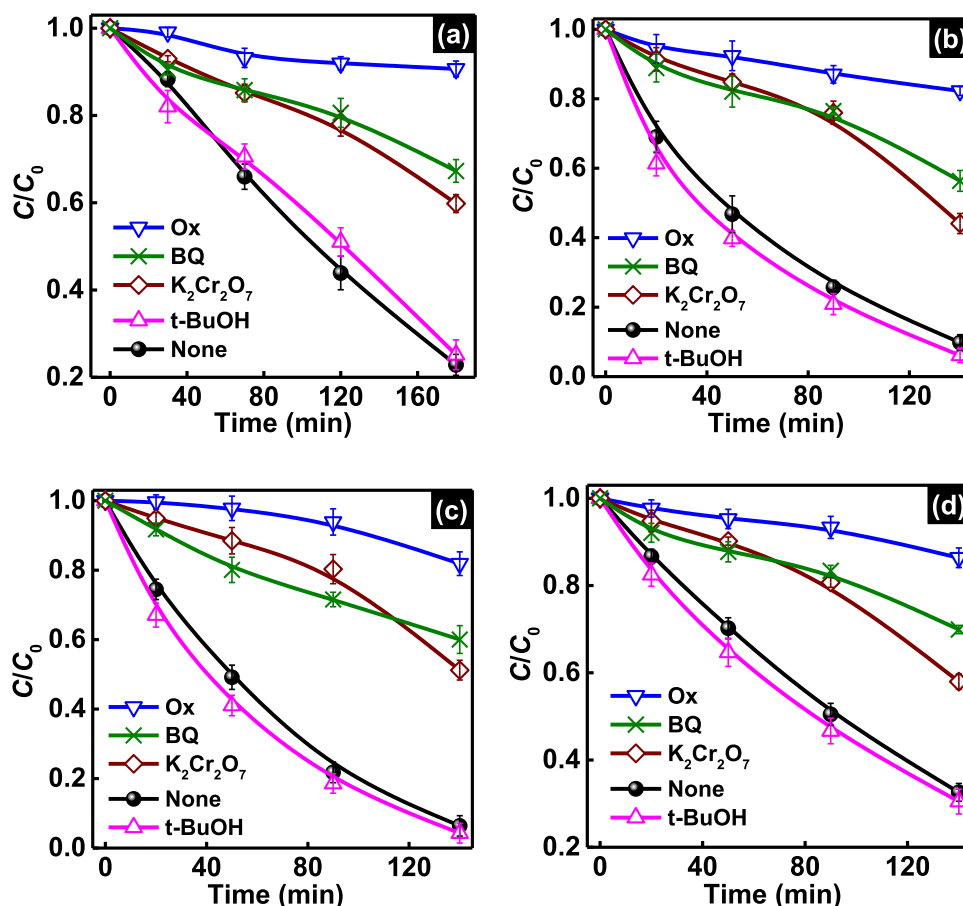


Fig. 7. Photocatalytic degradation of RhB on (a) Bi₂MoO₆, (b) Bi/Cu-3, (c) Bi/Co-2, and (d) Bi/Ni-2 with different scavengers: 20 mM *tert*-butyl alcohol (t-BuOH), 1 mM sodium oxalate (Ox), 10 mM K₂Cr₂O₇ and 0.1 mM benzoquinone (BQ).

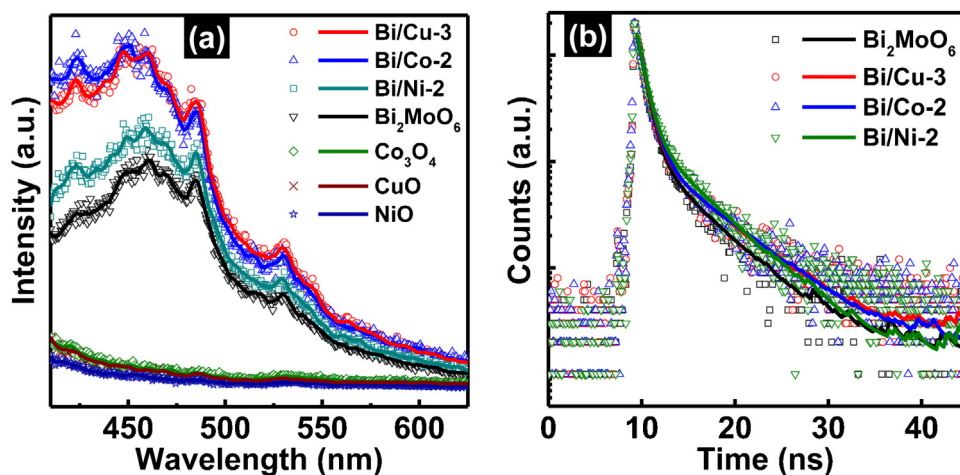


Fig. 8. (a) Photoluminescence and (b) time-resolved fluorescence decay spectra of Bi₂MoO₆, MO (M = Cu, Co₃/4, or Ni), and their composites. The curves in (b) were obtained by fitting the data to a two-exponential decay model.

junctions which usually show weakened PL intensity [29,70,71], but feature Z-scheme heterojunctions [14,69,72–75]. For the Z-scheme heterojunctions, the increase in PL intensity arises from the recombination of the photogenerated e^- at CB of the PC II and the h^+ at VB of the PC I [69,73].

To confirm the formation of the Z-scheme Bi₂MoO₆/MO heterojunctions, energy band levels of the Bi₂MoO₆ and MO were determined. As shown in Fig. 9a, Fermi levels (E_{f1-4} , vs NHE) of the Bi₂MoO₆, CuO, Co₃O₄, and NiO samples are calculated to be 0.63,

0.83, 0.10, and 0.53 eV, respectively, via the equation $E_f = \varphi - 4.44$ eV [19]. Distances ($E_{VB'}$) from VB edge levels (E_{VB} vs NHE) to the E_f for the four samples are determined to be 1.65, 0.68, 0.84, and 0.66 eV, respectively, from the VB XPS spectra (Fig. 10). Then the E_{VB} of them are figured out to be 2.28, 1.51, 0.94, and 1.19 eV, respectively, via the equation $E_{VB} = E_{VB'} + E_f$, and their corresponding CB edge levels (E_{CB} vs NHE) are calculated to be -0.20 , $+0.13$, -0.78 , and -1.31 eV, respectively, via the equation $E_{CB} = E_{VB} - E_g$.

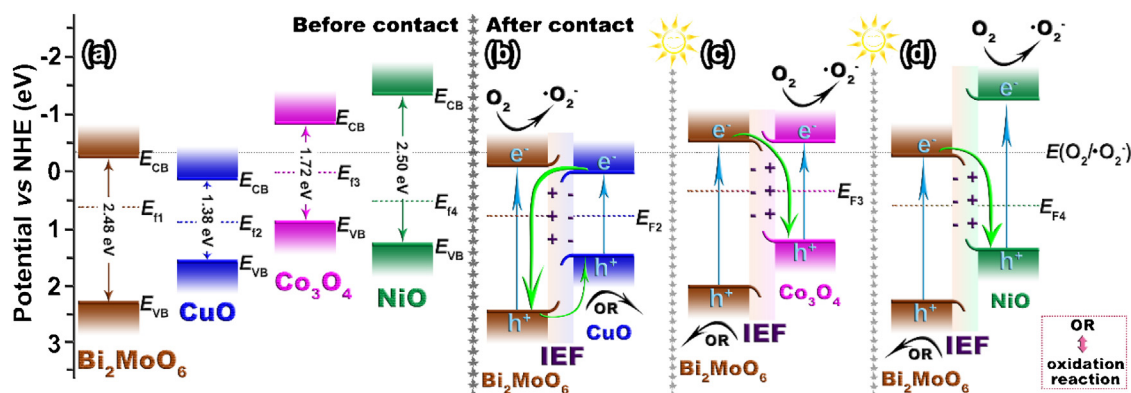


Fig. 9. Schematic illustrations for energy bands and charge transfer processes of Z-scheme $\text{Bi}_2\text{MoO}_6/\text{MO}$ ($\text{M} = \text{Cu}, \text{Co}_{3/4}, \text{or Ni}$) heterojunctions. IEF denotes internal electric field. E_{F1-4} are Fermi levels of Bi_2MoO_6 and MO. E_{F1-3} is united Fermi levels of $\text{Bi}_2\text{MoO}_6/\text{MO}$ heterojunctions.

Table 1

Fitting results of time-resolved fluorescence decay spectra (Fig. 8b) using a two-

exponential decay model $\text{Int}(t) = \sum_{i=1}^2 a_i e^{-t/\tau_i}$ where Int , τ_i and a_i are the intensity, the lifetime and the amplitude of the i th component, respectively.

Sample	τ_1/ns ($\text{Int}_1/\%$)	τ_2/ns ($\text{Int}_2/\%$)	χ^2
Bi_2MoO_6	0.794 (81.6)	4.970 (18.4)	1.337
Bi/Cu-3	0.842 (79.3)	5.641 (20.7)	1.390
Bi/Co-2	0.898 (78.7)	6.090 (21.3)	1.405
Bi/Ni-2	0.815 (75.4)	5.054 (24.6)	1.451

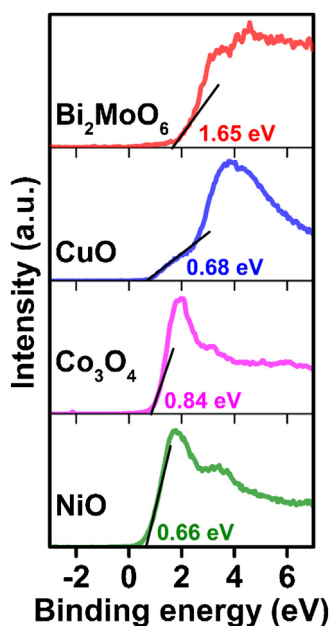


Fig. 10. VB XPS spectra of Bi_2MoO_6 and MO ($\text{M} = \text{Cu}, \text{Co}_{3/4}, \text{or Ni}$). The Fermi level is at 0 eV. Numbers in the figure are energy differences between VB edge levels and Fermi levels.

After contact of the Bi_2MoO_6 with the MO, the e^- transfers from the semiconductor with higher E_f to that with lower one, i.e. from Bi_2MoO_6 to CuO for $\text{Bi}_2\text{MoO}_6/\text{CuO}$, from Co_3O_4 to Bi_2MoO_6 for $\text{Bi}_2\text{MoO}_6/\text{Co}_3\text{O}_4$, and from NiO to Bi_2MoO_6 for $\text{Bi}_2\text{MoO}_6/\text{NiO}$, which is consistent with the XPS results. The e^- transfers cause shifts of the E_f toward each other and concomitant shifts of the E_{CB} and E_{VB} , until united E_f (E_{F1-3}) is formed (Fig. 9b–d). In this process, an IEF, with the same direction as the e^- transfer, is generated at the $\text{Bi}_2\text{MoO}_6/\text{MO}$ interface, and the IEF makes the energy

bands of photocatalysts bend at the interface (Fig. 9b–d). Under visible light irradiation, both the Bi_2MoO_6 and the MO can be excited. The IEF accelerates the e^- transfer from CB of CuO to VB of Bi_2MoO_6 for $\text{Bi}_2\text{MoO}_6/\text{CuO}$ (Fig. 9b), but from CB of Bi_2MoO_6 to VB of Co_3O_4 for $\text{Bi}_2\text{MoO}_6/\text{Co}_3\text{O}_4$ (Fig. 9c) or to VB of NiO for $\text{Bi}_2\text{MoO}_6/\text{NiO}$ (Fig. 9d), to recombine with the h^+ . Thereby, the charge carrier recombination rate in each semiconductor is considerably reduced, leaving more e^- to generate $\cdot\text{O}_2^-$ and more h^+ to directly oxidize the organics. Simultaneously, the IEF prohibits the e^- transfers between the CBs of the Bi_2MoO_6 and MO and the h^+ transfers between their VBs, except the $\text{Bi}_2\text{MoO}_6/\text{CuO}$ in which the h^+ can transfer from VB of the Bi_2MoO_6 to that of the CuO. On the whole, the IEF substantially increases the interfacial charge transfer rate between the Bi_2MoO_6 and MO, and the close contact between them (Fig. 2) probably leads to the formation of a quasi-Ohmic contact [8]. These form the Z-scheme heterojunctions. Though the E_{CB} of the Bi_2MoO_6 (Fig. 9a, b) is slightly lower than the reduction potential of O_2 ($E(\text{O}_2/\cdot\text{O}_2^-) = -0.33 \text{ eV}$ vs NHE, pH 7), the e^- at the VB can be excited to higher levels (e.g. $\sim 0.47 \text{ eV}$ higher than the E_{CB} under illumination of light with λ of 420 nm) to successfully reduce O_2 to $\cdot\text{O}_2^-$. The $\text{Bi}_2\text{MoO}_6/\text{Co}_3\text{O}_4$ and $\text{Bi}_2\text{MoO}_6/\text{NiO}$ Z-scheme heterojunctions possess high e^- reducibility of Co_3O_4 or NiO and high h^+ oxidizability of Bi_2MoO_6 , but the Z-scheme $\text{Bi}_2\text{MoO}_6/\text{CuO}$ heterojunctions only possess relatively high e^- reducibility of Bi_2MoO_6 , because the CB and VB levels of CuO lie in the forbidden band of Bi_2MoO_6 (Fig. 9a). On the whole, the formation of Z-scheme heterojunctions depend to a decisive extent on the energy band structures and interfacial IEFs of the samples.

According to above results, after two semiconductors contact, whether the Z-scheme heterojunctions or the traditional heterojunctions are formed depends on relative positions of their Fermi, CB, and VB levels. The relative positions of Fermi levels decide direction of the formed internal IEF, and those of the CB and VB levels influence transfer directions of the photogenerated e^- and h^+ . Therefore, it's necessary to measure the energy band levels of each component when studying heterojunction photocatalysts. The energy band shift, induced by the difference in Fermi levels, must be considered in order to well interpret the photocatalytic phenomena. For instance, if the energy band shifts of the Bi_2MoO_6 and CuO were neglected after they contact, the photogenerated e^- and h^+ would transfer from CB and VB of Bi_2MoO_6 to those of CuO, respectively, because the energy band levels of CuO lie in the forbidden band of Bi_2MoO_6 (Fig. 9a). This process does not favor the increase of SEPC and photoactivity, and thus is contradictory with the photocatalytic results (Fig. 6).

4. Conclusions

The solid-state Z-scheme $\text{Bi}_2\text{MoO}_6/\text{MO}$ photocatalysts were firstly prepared through facile calcination processes. The MO uniformly distributes on the surfaces of the Bi_2MoO_6 hierarchical microspheres, and distinct interfaces between the Bi_2MoO_6 and MO can be observed. As the energy band levels of the Bi_2MoO_6 and MO are determined, the electron transfers between the Bi_2MoO_6 and MO and the interfacial IEF, formed after the electron transfers, are verified. These Z-scheme photocatalysts exhibit higher photocatalytic performance, toward degradations of the RhB and SRhB, than the pure Bi_2MoO_6 and MO under visible light irradiation. The IEF plays a key role for the photoactivity enhancement. The h^+ and $\cdot\text{O}_2^-$ are primary active species. This work firstly illustrates the role of the interfacial IEF in photocatalytic processes of solid-state two-component Z-scheme heterojunctions, and provide better insight into the formation mechanism of these heterojunctions.

Acknowledgements

This work was supported financially by the National Natural Science Foundation of China (Nos. 21573133 and 21273135) and the Fundamental Research Funds of Shandong University in China (No. 12320075614004).

Appendix A. Supplementary data

Supplementary data associated with this article can be found, in the online version, at <http://dx.doi.org/10.1016/j.apcatb.2016.02.015>.

References

- [1] D. Kim, K.K. Sakimoto, D. Hong, P. Yang, *Angew. Chem. Int. Ed.* 54 (2015) 3259–3266.
- [2] H. Li, Y. Zhou, W. Tu, J. Ye, Z. Zou, *Adv. Funct. Mater.* 25 (2015) 998–1013.
- [3] L. Shi, L. Liang, F. Wang, J. Ma, J. Sun, *Catal. Sci. Technol.* 4 (2014) 3235–3243.
- [4] Y. Zheng, L. Lin, B. Wang, X. Wang, *Angew. Chem. Int. Ed.* 54 (2015) 12868–12884.
- [5] R. Asahi, T. Morikawa, H. Irie, T. Ohwaki, *Chem. Rev.* 114 (2014) 9824–9852.
- [6] J. Zhu, F. Fan, R. Chen, H. An, Z. Feng, C. Li, *Angew. Chem. Int. Ed.* 54 (2015) 9111–9114.
- [7] S.J.A. Moniz, S.A. Shevlin, D.J. Martin, Z.-X. Guo, J. Tang, *Energy Environ. Sci.* 8 (2015) 731–759.
- [8] P. Zhou, J. Yu, M. Jaroniec, *Adv. Mater.* 26 (2014) 4920–4935.
- [9] K. Iwashina, A. Iwase, Y.H. Ng, R. Amal, A. Kudo, *J. Am. Chem. Soc.* 137 (2015) 604–607.
- [10] L.J. Zhang, S. Li, B.K. Liu, D.J. Wang, T.F. Xie, *ACS Catal.* 4 (2014) 3724–3729.
- [11] H. Tada, T. Mitsui, T. Kiyonaga, T. Akita, K. Tanaka, *Nat. Mater.* 5 (2006) 782–786.
- [12] R. Abe, K. Shinmei, N. Koumura, K. Hara, B. Ohtani, *J. Am. Chem. Soc.* 135 (2013) 16872–16884.
- [13] D. Xu, B. Cheng, S. Cao, J. Yu, *Appl. Catal. B* 164 (2015) 380–388.
- [14] T.F. Yeh, C.Y. Teng, S.J. Chen, H. Teng, *Adv. Mater.* 26 (2014) 3297–3303.
- [15] X. Yang, H. Tang, J. Xu, M. Antonietti, M. Shalom, *ChemSusChem* 8 (2015) 1350–1358.
- [16] J. Jin, J. Yu, D. Guo, C. Cui, W. Ho, *Small* 11 (2015) 5262–5271.
- [17] Z. Huang, Q. Sun, K. Lv, Z. Zhang, M. Li, B. Li, *Appl. Catal. B* 164 (2015) 420–427.
- [18] H. Cheng, J. Hou, O. Takeda, X.-M. Guo, H. Zhu, *J. Mater. Chem. A* 3 (2015) 11006–11013.
- [19] J.C. Wang, L. Zhang, W.X. Fang, J. Ren, Y.Y. Li, H.C. Yao, J.S. Wang, Z.J. Li, *ACS Appl. Mater. Interfaces* 7 (2015) 8631–8639.
- [20] Y. Hong, Y. Jiang, C. Li, W. Fan, X. Yan, M. Yan, W. Shi, *Appl. Catal. B* 180 (2016) 663–673.
- [21] K. Kailasam, A. Fischer, G. Zhang, J. Zhang, M. Schwarze, M. Schroder, X. Wang, R. Schomacker, A. Thomas, *ChemSusChem* 8 (2015) 1404–1410.
- [22] W. Yu, D. Xu, T. Peng, *J. Mater. Chem. A* 3 (2015) 19936–19947.
- [23] F. Peng, Q. Zhou, D. Zhang, C. Lu, Y. Ni, J. Kou, J. Wang, Z. Xu, *Appl. Catal. B* 165 (2015) 419–427.
- [24] X. Chang, T. Wang, P. Zhang, J. Zhang, A. Li, J. Gong, *J. Am. Chem. Soc.* 137 (2015) 8356–8359.
- [25] Y. Ma, Y. Jia, Z. Jiao, M. Yang, Y. Qi, Y. Bi, *Chem. Commun.* 51 (2015) 6655–6658.
- [26] J. Bi, L. Wu, J. Li, Z. Li, X. Wang, X. Fu, *Acta Mater.* 55 (2007) 4699–4705.
- [27] J. Tian, P. Hao, N. Wei, H. Cui, H. Liu, *ACS Catal.* 5 (2015) 4530–4536.
- [28] Z. Dai, F. Qin, H. Zhao, F. Tian, Y. Liu, R. Chen, *Nanoscale* 7 (2015) 11991–11999.
- [29] H. Li, J. Liu, W. Hou, N. Du, R. Zhang, X. Tao, *Appl. Catal. B* 160–161 (2014) 89–97.
- [30] H. Li, Q. Deng, J. Liu, W. Hou, N. Du, R. Zhang, X. Tao, *Catal. Sci. Technol.* 4 (2014) 1028–1037.
- [31] W.N. Wang, F. Wu, Y. Myung, D.M. Niedzwiedzki, H.S. Im, J. Park, P. Banerjee, P. Biswas, *ACS Appl. Mater. Interfaces* 7 (2015) 5685–5692.
- [32] W. Fan, C. Zhang, H. Bai, X. Yu, W. Shi, *Eur. J. Inorg. Chem.* 2014 (2014) 3608–3613.
- [33] J. Zhang, C. Niu, J. Ke, L. Zhou, G. Zeng, *Catal. Commun.* 59 (2015) 30–34.
- [34] J. Lv, K. Dai, J. Zhang, L. Geng, C. Liang, Q. Liu, G. Zhu, C. Chen, *Appl. Surf. Sci.* 358 (2015) 377–384.
- [35] G. Tian, Y. Chen, W. Zhou, K. Pan, Y. Dong, C. Tian, H. Fu, *J. Mater. Chem.* 21 (2011) 887–892.
- [36] H. Li, T. Hu, J. Liu, S. Song, N. Du, R. Zhang, W. Hou, *Appl. Catal. B* 182 (2016) 431–438.
- [37] M. Zhang, C. Shao, J. Mu, X. Huang, Z. Zhang, Z. Guo, P. Zhang, Y. Liu, *J. Mater. Chem.* 22 (2012) 577–584.
- [38] F. Niu, D. Chen, L. Qin, N. Zhang, J. Wang, Z. Chen, Y. Huang, *ChemCatChem* 7 (2015) 3279–3289.
- [39] M.M. Natile, A. Glisenti, *Chem. Mater.* 15 (2003) 2502–2510.
- [40] J. Wu, Y. Xue, X. Yan, W. Yan, Q. Cheng, Y. Xie, *Nano Res.* 5 (2012) 521–530.
- [41] X. Yan, L. Tian, X. Chen, *J. Power Sources* 300 (2015) 336–343.
- [42] J.A. Rodriguez, J.C. Hanson, A.I. Frenkel, J.Y. Kim, M. Pérez, *J. Am. Chem. Soc.* 124 (2002) 346–354.
- [43] H.-q. Jiang, H. Endo, H. Natori, M. Nagai, K. Kobayashi, *Mater. Res. Bull.* 44 (2009) 700–706.
- [44] M. Nishibori, W. Shin, N. Izu, T. Itoh, I. Matsubara, *Catal. Today* 201 (2013) 85–91.
- [45] J.L. Rodríguez, M.A. Valenzuela, T. Poznyak, L. Lartundo, I. Chairez, J. Hazard. Mater. 262 (2013) 472–481.
- [46] H.J. Freund, H. Behner, B. Bartos, G. Wedler, H. Kühlenbeck, M. Neumann, *Surf. Sci.* 180 (1987) 550–564.
- [47] X.-Y. Yu, R.-X. Xu, C. Gao, T. Luo, Y. Jia, J.-H. Liu, X.-J. Huang, *ACS Appl. Mater. Interfaces* 4 (2012) 1954–1962.
- [48] Z. Zhang, C. Shao, X. Li, Y. Sun, M. Zhang, J. Mu, P. Zhang, Z. Guo, Y. Liu, *Nanoscale* 5 (2013) 606–618.
- [49] M. Sathish, B. Viswanathan, R.P. Viswanath, C.S. Gopinath, *Chem. Mater.* 17 (2005) 6349–6353.
- [50] C. Lv, G. Chen, J. Sun, Y. Zhou, S. Fan, C. Zhang, *Appl. Catal. B* 179 (2015) 54–60.
- [51] Z. Kang, X. Yan, L. Zhao, Q. Liao, K. Zhao, H. Du, X. Zhang, X. Zhang, Y. Zhang, *Nano Res.* 8 (2015) 2004–2014.
- [52] D.-J. Yun, Y.-J. Jeong, H. Ra, J.-M. Kim, T.K. An, M. Seol, J. Jang, C.E. Park, S.-W. Rhee, D.S. Chung, *J. Mater. Chem. C* 3 (2015) 7325–7335.
- [53] J.-E. Lee, N.T. Khoa, S.W. Kim, E.J. Kim, S.H. Hahn, *Mater. Chem. Phys.* 164 (2015) 29–35.
- [54] X.-D. Yang, L.-L. Jiang, C.-J. Mao, H.-L. Niu, J.-M. Song, S.-Y. Zhang, *Mater. Lett.* 115 (2014) 121–124.
- [55] M. Long, W. Cai, H. Kisch, *Chem. Phys. Lett.* 461 (2008) 102–105.
- [56] A. Nashim, S. Martha, K.M. Parida, *RSC Adv.* 4 (2014) 14633–14643.
- [57] J. Park, X. Shen, G. Wang, *Sensor Actuat. B* 136 (2009) 494–498.
- [58] F. Davar, Z. Fereshteh, M. Salavati-Niasari, *J. Alloy Compd.* 476 (2009) 797–801.
- [59] Y.-S. Xu, W.-D. Zhang, *Dalton Trans.* 42 (2013) 1094–1101.
- [60] C.-Y. Chiang, Y. Shin, K. Aroh, S. Ehrman, *Int. J. Hydrogen Energy* 37 (2012) 8232–8239.
- [61] Q. Yan, X. Li, Q. Zhao, G. Chen, *J. Hazard. Mater.* 209–210 (2012) 385–391.
- [62] M.D. Irwin, D.B. Buchholz, A.W. Hains, R.P.H. Chang, T.J. Marks, *Proc. Natl. Acad. Sci. U. S. A.* 105 (2008) 2783–2787.
- [63] S. Hüfner, *Adv. Phys.* 43 (1994) 183–356.
- [64] X. Xiao, R. Hu, C. Liu, C. Xing, C. Qian, X. Zuo, J. Nan, L. Wang, *Appl. Catal. B* 140–141 (2013) 433–443.
- [65] L. Mohapatra, K. Parida, M. Satpathy, *J. Phys. Chem. C* 116 (2012) 13063–13070.
- [66] S. Ge, L. Zhang, *Environ. Sci. Technol.* 45 (2011) 3027–3033.
- [67] S. Cho, J.-W. Jang, K.-j. Kong, E.S. Kim, K.-H. Lee, J.S. Lee, *Adv. Funct. Mater.* 23 (2013) 2348–2356.
- [68] X. Wang, C. Liow, A. Bisht, X. Liu, T.C. Sum, X. Chen, S. Li, *Adv. Mater.* 27 (2015) 2207–2214.
- [69] W. Tu, Y. Zhou, S. Feng, Q. Xu, P. Li, X. Wang, M. Xiao, Z. Zou, *Chem. Commun.* 51 (2015) 13354–13357.
- [70] H. Li, W. Hou, X. Tao, N. Du, *Appl. Catal. B* 172–173 (2015) 27–36.
- [71] H. Li, J. Shang, Z. Ai, L. Zhang, *J. Am. Chem. Soc.* 137 (2015) 6393–6399.
- [72] S. Chen, Y. Hu, S. Meng, X. Fu, *Appl. Catal. B* 150–151 (2014) 564–573.
- [73] S. Meng, X. Ning, T. Zhang, S.F. Chen, X. Fu, *Phys. Chem. Chem. Phys.* 17 (2015) 11577–11585.
- [74] J. Zhang, Y. Hu, X. Jiang, S. Chen, S. Meng, X. Fu, *J. Hazard. Mater.* 280 (2014) 713–722.
- [75] X. Wang, G. Liu, Z.G. Chen, F. Li, L. Wang, G.Q. Lu, H.M. Cheng, *Chem. Commun.* (2009) 3452–3454.